JOURNAL OF GEOPHYSICAL RESEARCH, VOL. 102, NO. B11, PAGES 24,589-24,603, NOVEMBER 10, 1997

Kinematics of postseismic relaxation from aftershock focal mechanisms of the 1994 Northridge, California, earthquake

Jeffrey R. Unruh
William Lettis & Associates, Walnut Creek, California

Robert J. Twiss
Department of Geology, University of California, Davis

Egill Hauksson
Seismological Laboratory, California Institute of Technology, Pasadena

Abstract. Geodetic observations of surface deformation associated with the 1994 Northridge, southern California, earthquake generally are reproduced by simple models of a large-scale elastic dislocation on a blind or buried thrust fault. The smaller-scale aftershocks of the Northridge earthquake are distributed throughout much of the volume of crust that appears to have deformed elastically during the mainshock. These aftershocks, averaged over volumes that are large relative to their rupture radii, reflect a distributed, permanent deformation that is accommodated by local brittle fracture. We use a micropolar continuum model to invert the aftershocks in such volumes for the average incremental strain, and we compare that deformation both with the elastic strain from the dislocation model of the mainshock and with geodetically measured strain. Aftershock deformation that occurred at depths below about 6 km, and which is associated with the primary rupture zone, is consistent with slow continuation of the southwest-side-up reverse slip on the blind Northridge thrust fault. In contrast, aftershock deformation from the upper 5-7 km of the hanging wall block directly above the thrust fault can be characterized by horizontal NE-SW shortening and horizontal NW-SE (i.e., fault-parallel) extension. This pattern of deformation is similar to that associated with the mainshock, as observed geodetically and as calculated from the elastic dislocation model. We interpret that the aftershock activity in the hanging wall represents the quasi-ductile accommodation by brittle deformation mechanisms of a permanent strain distributed through the hanging wall block. The aftershocks along the mainshock rupture zone are interpreted as resulting from either (1) the time-dependent release along a weakened fault zone of part of the remaining accumulated elastic strain in the upper crust or (2) the continued slip in the weakened fault zone driven by the deformation of a ductile-elastic lower crustal layer that relaxes under the stress transferred by the coseismic loss of cohesion in the upper crust. In either case, the aftershock activity suggests that the crust undergoes quasi-ductile flow as a brittle-elastic material, and is not a strictly elastic material.

1. Introduction

In this paper we use a generalized continuum model to evaluate distributed brittle deformation accommodated by aftershocks of the 1994 Northridge earthquake, which occurred on a blind thrust fault beneath the western Transverse Ranges in southern California (Figure 1). Patterns of regional deformation associated with the mainshock have been investigated by several workers [*Hudnut et al.*, 1996; *Wald et al.*, 1996; *Shen et al.*, 1996], primarily through analysis of coseismic surface displacements measured by geodetic techniques. The modeling approach favored by these workers assumes that the mainshock rupture can be approximated by a dislocation within an elastic material, and it consists of finding a combination of elastic strength, fault geometry, and slip distribution that best reproduces the geodetically determined surface displacements. The success of these models in reproducing the first-order pattern of surface deformation [*Hudnut et al.*; 1996, *Wald et al.*, 1996; *Shen et al.*, 1996] provides reasonable justification for the assumption that the upper crust deformed elastically in the vicinity of the slip dislocation that caused the earthquake.

Aftershocks of the Northridge earthquake are not confined to a single plane but rather are distributed throughout much of the volume of crust that responded elastically to the mainshock rupture (Figures 2 and 3). Each aftershock represents a discrete displacement event on a fault surface; also, each aftershock is roughly one or more orders of magnitude smaller than the mainshock. If we consider a

Paper number 97JB02157.
0148-0227/97/97JB-02157$09.00

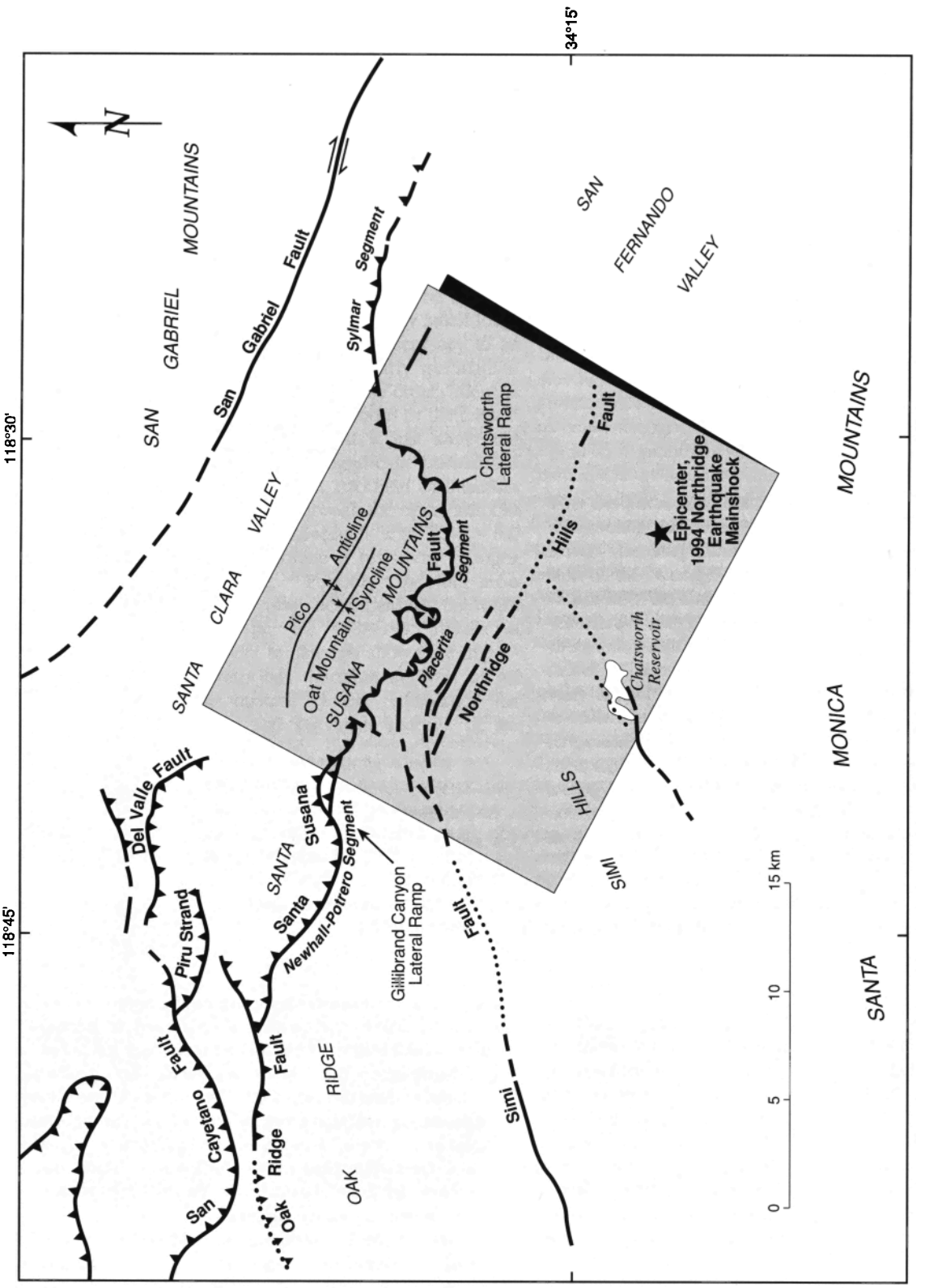

Figure 1. Late Cenozoic contractional structures in the vicinity of the Northridge earthquake (modified from *Jennings and Strand* [1969], *Yeats* [1987], and *Yeats et al.* [1994]). Lateral ramps in the Santa Susana fault mark the boundaries of structural segments in the Santa Susana Mountains defined by *Yeats et al.* [1994] (see text for details). Shaded region shows location of the blind, southwest dipping Northridge thrust [from *Wald et al.*, 1996].

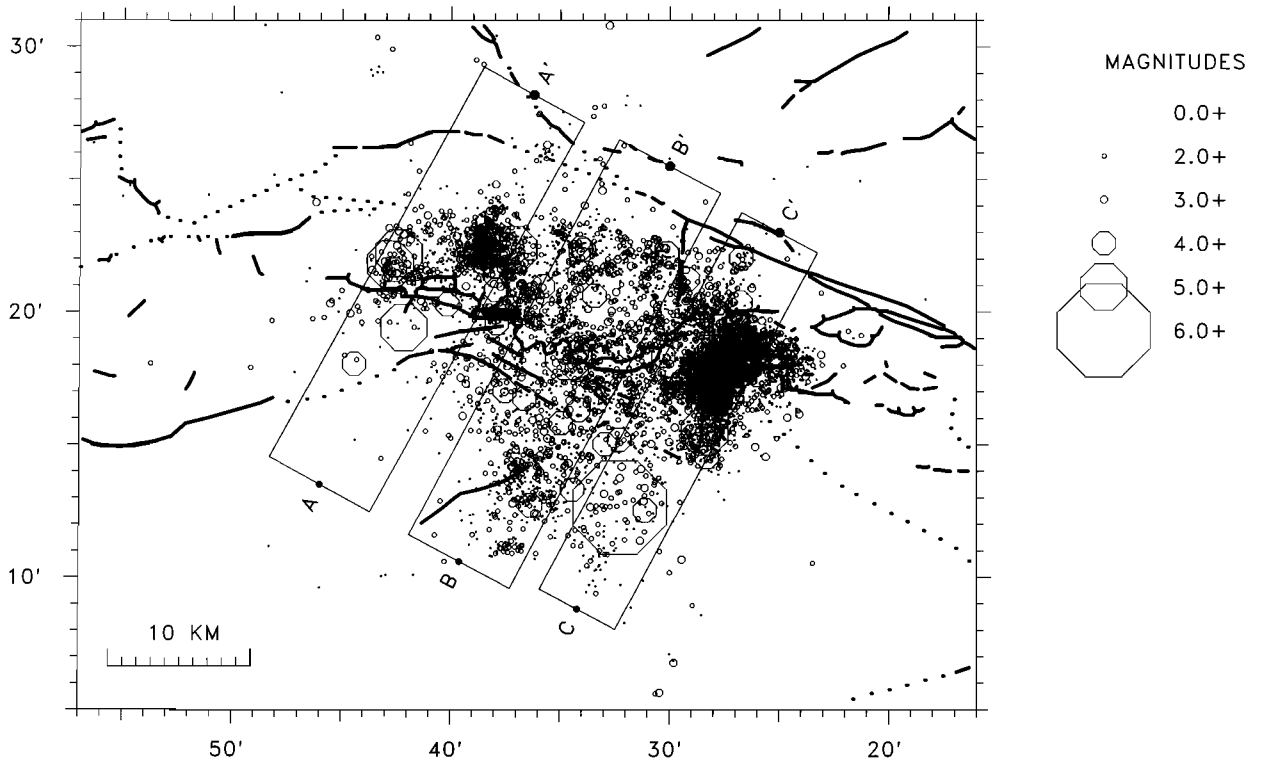

Figure 2. Epicenter map of the 1994 Northridge earthquake aftershocks.

volume of crust that is large relative to the rupture radius of an individual aftershock but small relative to the rupture radius of the mainshock, then the gradual accumulation of aftershocks within the volume, when smoothed over the volume and over time, constitutes a quasi-ductile deformation of the volume. *Kostrov* [1974] refers to such a deformation as a "seismic flow," and structural geologists commonly refer to a deformation accommodated by distributed brittle fracture as a "cataclastic flow."

The goal of this paper is to use a continuum model to invert the aftershocks for the characteristics of the seismic flow accommodated by the Northridge earthquake aftershocks and to compare this deformation both with the theoretically modeled elastic deformation and with the geodetically measured deformation associated with the mainshock. In the following sections we first describe the geologic setting of the earthquake, the elastic models of the mainshock deformation, and the patterns of aftershock activity. We then describe the kinematic basis for the generalized continuum model and the analytic approach used to invert aftershock focal mechanisms for the characteristics of the seismic flow. We present the results of our analysis and interpret the significance of the aftershock deformation for relaxation of the coseismic elastic strain and for kinematic models that describe progressive contractional deformation of crystalline basement terranes.

2. Geologic Setting of the Northridge Earthquake

The blind thrust fault that produced the Northridge earthquake dips southwest beneath the southern margin of the east Ventura basin and the northern San Fernando Valley [*Hauksson et al.*, 1995]. *Huftile and Yeats* [1996] named this fault the "Northridge thrust." The upper part of the Northridge thrust underlies a belt of southwest vergent contractional structures exposed in the Santa Susana mountains and the southern Santa Clara Valley (Figure 1). The leading edge of this contractional belt is the Santa Susana thrust fault, which dips northeast beneath the Santa Susana Mountains and the eastern Ventura basin. The footwall of the Santa Susana thrust is interpreted to be involved in development of a northeast vergent fold or basement uplift above the southwest dipping Northridge thrust [*Davis and Namson*, 1994; *Yeats and Huftile*, 1994; *Huftile and Yeats*, 1996].

The hanging wall of the Santa Susana thrust contains south to southwest vergent contractional structures that appear in the Santa Susana Mountains and are bounded to the northeast by the San Gabriel fault. These structures were grouped into the Sylmar, Placerita, and Newhall-Potrero structural segments by *Yeats et al.* [1994] based primarily on the presence of lateral ramps in the trace of the Santa Susana thrust (e.g., the Gillibrand Canyon and Chatsworth lateral ramps [*Yeats*, 1987] and on variations in structural style in the hanging wall of the thrust (Figure 1).

Although the fold and thrust structures mapped at the surface (Figure 1) are expressed in deformed Cenozoic strata, the underlying thrust faults are rooted in Mesozoic crystalline basement rocks that underlie the east Ventura basin and the northern San Fernando Valley [*Hauksson and Haase*, 1997]. Drill hole data presented by *Huftile and Yeats* [1996] show that the Cenozoic cover on the crystalline basement beneath the east Ventura basin is approximately 4 km or less in thickness. Because aftershocks of the Northridge earthquake show that the seismogenic thrust fault extends to a depth of about 21 km and that most of the coseismic slip occurred beneath 10 km depth [*Wald et al.*, 1996], we anticipate that the average rheology of the hanging wall is most strongly influenced the crystalline

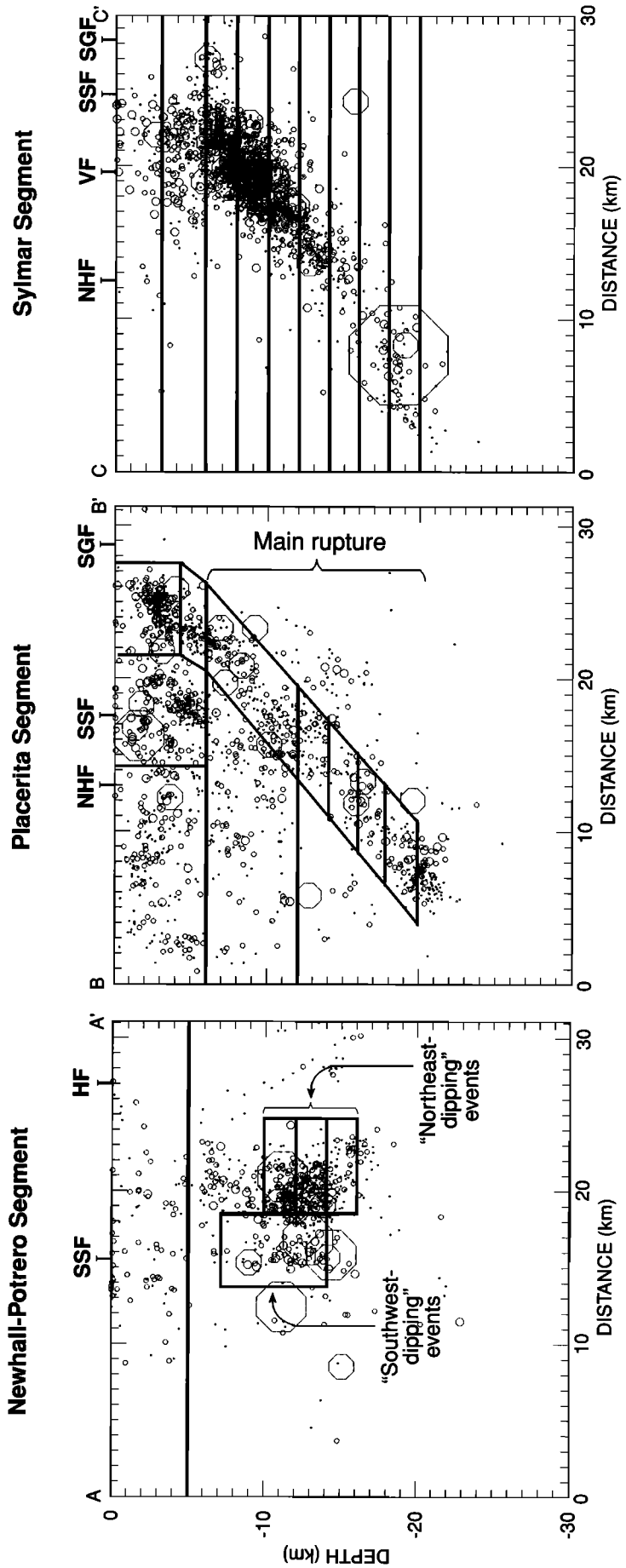

Figure 3. Cross sections of hypocenters of Northridge earthquake aftershocks (see Figure 2 for locations of section lines).

basement beneath the Cenozoic cover. Thus the major map-scale contractional structures in the region (e.g., the Santa Monica Mountains and Santa Susana Mountains anticlinoria [*Davis and Namson*, 1994] probably are best characterized as basement-involved uplifts or anticlines [*Narr and Suppe*, 1994].

3. Coseismic Deformation and Elastic Models

Patterns of surface deformation associated with the Northridge earthquake have been determined from Global Positioning System (GPS) geodesy [*Hudnut et al.*, 1996]. These studies show an approximately symmetrical pattern of coseismic displacements in the vicinity of the epicenter: GPS stations to the northeast and southwest of the epicentral region moved toward each other, accommodating horizontal shortening normal to the strike of the Northridge thrust fault, and stations to the northwest and southeast of the epicentral region moved away from each other, accommodating horizontal lengthening parallel to the strike of the fault. These motions are illustrated by particle displacement paths sketched parallel to the displacement directions of the GPS stations (Figure 4). Although the fault-normal shortening is not surprising given the dip-slip motion on the Northridge thrust, the fault-parallel lengthening is not accounted for in two-dimensional kinematic models for finite growth of basement-involved anticlines [e.g., *Narr and Suppe*, 1994].

The observed pattern of coseismic displacements, including the fault-parallel lengthening, is reproduced by models that approximate the Northridge earthquake as a dislocation on a

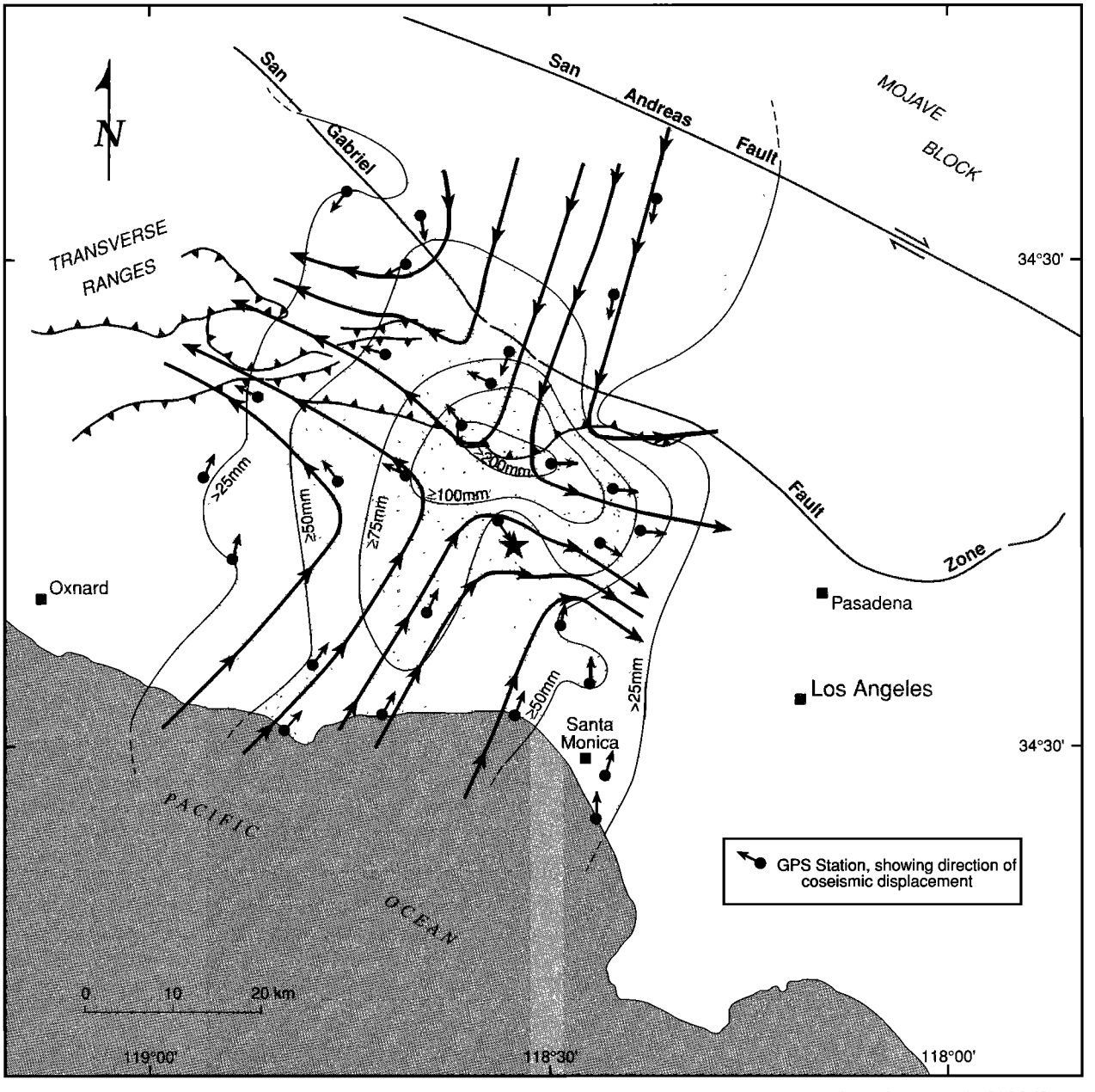

Figure 4. Displacement of GPS stations during the Northridge earthquake (from data of *Hudnut et al.* [1996]). Displacement directions are shown by arrows attached to individual GPS stations. Magnitude of horizontal displacement is indicated by contour lines. Interpreted particle displacement paths are sketched parallel to the coseismic displacement directions to indicate the patterns of crustal flow during the mainshock rupture.

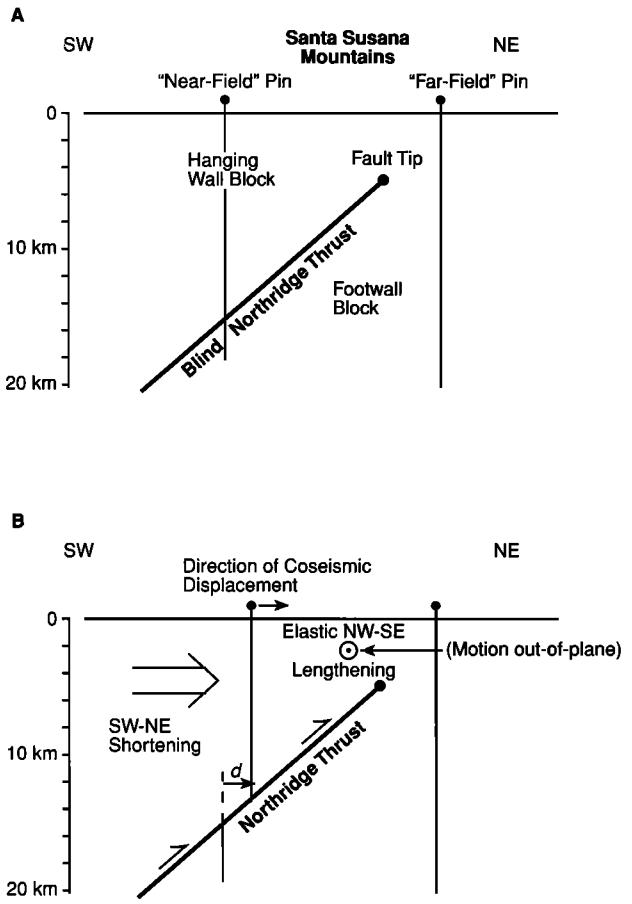

Figure 5. Model for the fault-parallel extensional strains indicated by geodetic measurements of coseismic deformation (Figure 4). (a) Structural relationships prior to the earthquake. (b) Coseismic slip on the blind Northridge thrust imposes a shortening on the hanging wall block in the direction of slip. The elastic response of the crust to the fault-normal shortening is a fault-parallel lengthening, which creates components of motion out of the plane that contains the slip vector.

buried or blind fault in an elastic material [*Hudnut et al.*, 1996; *Shen et al.*, 1996; *Wald et al.*, 1996]. The northeast directed motion of the hanging wall block during the earthquake is the result of simple shearing along the Northridge thrust fault. Because the fault does not break the surface, however, the northeast directed motion of the hanging wall block must be accommodated by a shortening strain normal to the strike of the fault (Figure 5). The modeled elastic response of the crust to this shortening is a northwest-southeast elongation parallel to the fault, which accounts for the observed pattern of fault-parallel motions (Figure 5). As shown by the coseismic displacement field (Figure 4), the magnitude of the fault-parallel extension is comparable to the fault-normal shortening in the region directly north of the mainshock. The near-field elastic deformation of the hanging wall block associated with the mainshock rupture thus can be characterized as an inhomogeneous, approximately horizontal pure shear strain; that is, the directions of maximum shortening and maximum lengthening are both subhorizontal and are directed normal to and parallel to, respectively, the strike of the fault.

4. Northridge Earthquake Aftershocks

Aftershocks of the Northridge earthquake (Figures 2 and 3) outline the geometry of the mainshock rupture zone [*Hauksson et al.*, 1995] and exhibit systematic variations that coincide with the structural segments in the Santa Susana Mountains identified by *Yeats et al.* [1994]. The Northridge thrust is relatively well-defined in the Sylmar segment southeast of the Chatsworth lateral ramp by a single southwest dipping zone of aftershocks (Figure 3, C-C'). The aftershocks extend to a depth of approximately 20 km and can be traced upward as a relatively planar, 3.5 km wide zone to a depth of approximately 7 km. Above this depth, aftershocks appear to be more diffuse and the mainshock rupture zone is difficult to identify as a discrete, well-defined structure.

In the Placerita segment between the Chatsworth and Gillibrand Canyon lateral ramps, the Northridge thrust appears to be well-defined by aftershocks between approximately 21 km and 12 km depth, but at shallower depths the seismicity appears to be distributed in the hanging wall (Figure 3, B-B'). *Shen et al.* [1996] noted that the mainshock rupture zone appears to steepen above approximately 9-10 km depth in this region, consistent with the observation of *Hauksson et al.* [1995] that the Gillibrand Canyon and Chatsworth lateral ramps bound a "ridge" in the base of the aftershock zone that is 3-5 km higher than the surrounding regions to the northwest and southeast.

In the Newhall-Potrero segment northwest of the Gillibrand Canyon lateral ramp, aftershocks suggest two oppositely dipping zones between approximately 10-17 km depth (Figure 3, A-A'): a southwest dipping zone to the south, and a northeast dipping zone to the north. It is not clear from patterns of aftershocks if one zone overlaps the other or if both terminate at approximately the same depth. There appear to be fewer aftershocks in the upper 9 km of the crust northwest of the Gillibrand Canyon lateral ramp (Figure 3, A-A').

5. Continuum Model for Evaluating Distributed Aftershock Deformation

The majority of the Northridge earthquake aftershocks are small magnitude ($M1$-$M3$) events with rupture dimensions of the order of a few tens to a few hundreds of meters. We wish to evaluate the average deformation of volumes of crust that are much larger than the rupture radius of an individual aftershock, so that the small coseismic displacements within a given volume collectively can be assumed to approximate a continuous deformation. This assumption is reasonable given the scattered distribution of most of the Northridge aftershocks, especially those that occurred in the hanging wall block above the primary rupture zone (Figure 3).

We use a micropolar continuum model [*Eringen*, 1966, 1967] to evaluate the characteristics of the brittle aftershock deformation. In contrast to classical continuum theory, which does not explicitly account for the substructure of a deforming, brittle material, the micropolar model assumes that the crust deforms like a granular material, where the "grains" are rigid, fault-bounded blocks that have dimensions comparable to the rupture radii of aftershocks [*Twiss et al.*, 1993]. The micropolar theory relates the instantaneous direction of shear along the boundaries of the "grains" to the larger-scale deformation of the material and to the local rotation of the

fault blocks. If the deformation is progressive and can be smoothed over time, it can be approximated as a rate of quasi-ductile flow and a rate of local block rotation. Any set of aftershock data then reflects an increment of that deformation that accumulates over a geologically small but finite time period.

The kinematics of a "granular" style of deformation are illustrated by the following example. The average deformation of a specific volume of crust can be characterized uniquely by the lengths and orientations of the three principal axes of the strain ellipsoid. This average deformation, however, is accommodated at a much smaller scale by the shearing of crustal blocks (i.e., "grains") past one another along their boundaries. The average motion of the block centroids can be described by a continuum approximation, and at any given time it defines the large-scale strain (i.e., change in shape) of the crustal volume. The relative motion of the block centroids in turn prescribes one component of the local direction of shearing along the block surfaces. Because the blocks are rigid and not physically attached to each other, they also are free to rotate about their centroids in a manner dictated by the local geometry of the blocks and their interactions with neighboring blocks. This local rotation contributes another component of shearing along the block boundaries, although it contributes nothing to the large-scale strain of the volume. To relate the local direction of shear along the block boundaries to the large-scale deformation of the volume, we need to explicitly account for the relative displacement of the block centroids as well as the local, small-scale rotations of the blocks about their centroids.

There are numerous, well-documented examples in the geologic literature of natural brittle deformations that include local rotation of fault-bounded blocks (see discussion of *Twiss et al.* [1993]). It is reasonable to assume that such deformations may be accommodated by earthquakes, which represent discrete slip events along the boundaries of rigid, fault-bounded blocks. The focal mechanisms that we use as kinematic data for our inversions are essentially data on the orientation of the two nodal planes, which are the possible shear planes, and the associated slip direction on each plane. According to the micropolar theory, the slip direction on any given surface is determined by two kinematic components: (1) the average large-scale deformation rate represented by the relative motion of the centroids of the rigid blocks, and (2) a local independent rotation rate of the individual blocks about their centroids [*Twiss et al.*, 1993]. In technical terms, the large scale deformation rate (i.e., the rate of change in shape of the crustal volume) is the symmetric part of the velocity gradient tensor (the strain rate) for a continuum defined by the centroids of the rigid blocks that constitute the material. The relative rotation rate (the relative vorticity) is basically the difference between the antisymmetric part of this velocity gradient tensor and the spin tensor that defines the independent local rotation rate of the rigid blocks. Thus use of the micropolar continuum model to interpret fault-slip data provides a better constraint on the characteristics of the strain rate, and also permits the extraction of additional kinematic information about the contributions of block rotations to patterns of slip on fault surfaces (see discussion and examples of *Unruh et al.* [1996]).

The micropolar theory is formulated in terms of rates because this is the appropriate form for kinematic variables in the constitutive equations describing ductile deformation [*Twiss et al.*, 1991, 1993]. The focal mechanisms provide constraints only on the directions of incremental slip on faults but not the actual slip magnitudes. Thus our inversions provide solutions only for the orientations of the principal incremental strain axes and for their relative magnitudes; the inversions do not constrain the actual magnitudes of the principal strains. The incremental strain tensor, however, can be converted into the strain rate tensor simply by dividing each of the incremental strain components by the same time increment, which is a scalar quantity. Dividing a tensor by a scalar affects neither the orientation of the principal axes nor the ratios (or ratios of differences) of the principal values. Thus conclusions about these characteristics of the incremental strain tensor also apply to the strain rate tensor. To avoid confusion in discussing the data, we will refer to the theoretically defined rates as if they were infinitesimal increments in the kinematic variables. To relate the terminology to the theory, it is only necessary to consider the infinitesimal increments as increments per unit time.

6. Analytical Approach

To relate the individual aftershocks to a large-scale strain increment and a small-scale relative rotation increment, we make the explicit assumption that the local coseismic slip occurs in the direction of the maximum resolved shear increment on fault surface and that the shear increment is the net result of the large-scale incremental strain tensor and the local incremental relative rotation. Our analytical approach then consists of two main steps: (1) group the focal mechanisms into discrete spatial domains of essentially homogeneous deformation; and (2) use the micropolar continuum model described above as a basis to invert the focal mechanisms for the incremental strain and incremental relative block rotation in each domain.

Data used for the inversions in this study consist of focal mechanisms for the Northridge aftershocks. These data were recorded by the Southern California Seismographic Network, a joint project of the California Institute of Technology and the U.S. Geological Survey. The methodology for determining focal mechanisms is described by *Hauksson et al.* [1995].

We grouped the focal mechanisms by spatial domains in order (1) to separate events on the primary rupture zone from aftershocks that were distributed within the hanging wall block; and (2) to analyze possible variations in seismogenic deformation associated with distinct structural segments of the contractional belt in the Santa Susana mountains. Our initial approach was to use the structural segments defined by *Yeats et al.* [1994] as a basis for grouping aftershocks (Figure 1). This appears reasonable, given the changes in geometry of the base of the aftershock zone associated with the Gillibrand Canyon and Chatsworth lateral ramps [*Hauksson et al.*, 1995]. Additional subdivisions of the data were performed as appropriate to isolate volumes of relatively homogeneous deformation.

Seismic P and T axes are unit vectors that conveniently describe the orientations of the nodal planes and the directions of the first motions. We calculated the P and T axes for the focal mechanism data and plotted them on equal-area, lower hemisphere, Kamb contour plots. The plots were inspected visually to assess the orientation and distribution of the P and T axes. If we determined that the P and T axes formed well-defined, single maxima on the Kamb plots, then we concluded

Table 1. Inversion Results, Sylmar Segment

Depth, km	d_1 (Maximum Extension)*	d_3 (Maximum Shortening)*	D	W	Mean Cos	$\cos^{-1}$ (Mean Cos)	Number of Data
0-3	98, 31	352, 24	0.5	0	0.983	10.616	39
3-6	143, 69	22, 11	0.5	0	0.968	14.419	202
6-8	54, 75	20, -12	0.5	0.1	0.979	11.756	306
8-10	35, 77	20, -12	0.5	0	0.987	9.381	181
10-12	310, 52	35, -4	0.5	0	0.988	8.955	158
12-14	295, 47	40, 14	0.5	0	0.987	9.293	142
14-16	172, 69	32, 16	0.6	0	0.982	10.767	85
16-18	312, 83	357, -5	0.5	0.1	0.975	12.778	28
18-20	214, 81	15, 8	0.6	-0.2	0.984	10.176	44

See text for complete descriptions of kinematic variables and misfit values.
*Orientations of d_1 and d_3 given as trend, followed by plunge. Positive values of plunge are below the horizontal; negative values are above the horizontal.

that the data reflect a homogeneous deformation within the volume of crust containing those aftershocks. For Kamb plots that showed multiple concentrations of P and/or T axes, however, we redefined the boundaries of the crustal volumes as appropriate until the associated Kamb plots showed that P and T axes clustered in distinct, well-defined maxima and thus reflected a more homogeneous deformation.

The inversion solution consists of finding the values of the model parameters for a micropolar deformation that minimize the misfit between the theoretically calculated P and T axes and the observed aftershock P and T axes. The five parameters of a micropolar model include (1) the three independent parameters that define the orientations of the principal axes of the strain rate, or incremental strain, tensor (d_1, maximum lengthening; d_3, maximum shortening; d_2, intermediate principal axis); (2) a scalar parameter D (the deformation rate parameter), defined by a ratio of the differences in the principal strain rates, or incremental strains, which characterizes the shape of the incremental strain ellipsoid,

$$D \equiv \frac{d_2 - d_3}{d_1 - d_3}; \tag{1}$$

and (3) a scalar parameter W which characterizes the relative vorticity (i.e., rate of relative rotation), of rigid, fault-bounded blocks about an axis parallel to d_2 [*Twiss et al.*, 1993]

$$W \equiv \frac{(\omega_{13} - w_{13})}{0.5(d_1 - d_3)} \tag{2}$$

where w_{13} is a component of the antisymmetric part of the large scale velocity gradient tensor which describes the average large-scale rotation rate about d_2 and ω_{13} is an independent component describing the local block rotation rate about d_2. As discussed previously, the parameter W can be interpreted to reflect the incremental relative rotation of fault-bounded blocks. As a first approximation, we ignore components of the relative vorticity about the other principal axes.

From any given set of micropolar model parameters, we can calculate the orientation of the P and T axes for any given orientation of shear plane [*Twiss et al.*, 1993; *Unruh et al.*, 1996]. For each observed pair of P and T axes representing an aftershock focal mechanism, we find the orientation of the model shear plane for which the model P and T axes are a best fit to the observed P and T axes. The misfit is taken to be the cosine of the unique rotation angle that brings the model P and T axes into coincidence with the observed P and T axes. The average of these misfits over all the focal mechanisms in the data set defines the mean cosine misfit, and we search for the model parameters that minimize this average misfit. In Tables 1-3 we report the average misfit as the angle whose cosine is the mean cosine misfit (i.e., $\cos^{-1}$(mean cosine misfit)).

We use a grid-search algorithm to find the parameters of the best fit micropolar model for each group of P and T axes. A discussion of our grid-search algorithm PTGRDSRCH and the rationale for the misfit calculation are discussed in detail by *Unruh et al.* [1996] and will not be repeated here. In general, we do not search the entire five-dimensional grid systematically because of the large amounts of computer time that would be required. Instead, we generally search a swath around the path that leads from the starting model to the final solution by taking the minimum misfit model in any subgrid as the central point in defining the subsequent subgrid and decreasing the size of the subgrid spacing as we approach the solution. We ensure that the minimum is bracketed for all parameters in the grid search. The best fit models are determined within grid increments of 5° for the orientation of the principal strain axes and within grid increments of 0.1 for the values of D and W. The corresponding precision of the solutions presented in Tables 1-3 are a grid resolution of ±2.5° for the orientations of d_1 and d_3, and a grid resolution of ±0.05 for the values of D and W.

7. Inversion Results

7.1. Seismogenic Deformation Along the Mainshock Rupture Zone

The inversion results (Tables 1-3; see Figures 2 and 3 for locations of depth domains cited in the tables) show that the aftershocks along the main rupture zone generally accommodate northeast-southwest shortening (i.e., d_3 is subhorizontal and oriented NE-SW) and vertical crustal thickening (i.e., the direction of maximum lengthening d_1 is steeply plunging to subvertical). This is consistent with southwest-side (i.e., hanging wall block) up simple shear on the primary rupture zone. In general, values of the deformation parameter D associated with the primary rupture zone are 0.5, which implies, for a constant volume deformation, that there

Table 2. Inversion Results, Placerita Segment

Depth, km	d_1 (Maximum Extension)*	d_3 (Maximum Shortening)*	D	W	Mean Cos	Cos^{-1} (Mean Cos)	Number of Data
			Primary Rupture Zone				
6-12	170, 72	26, 15	0.6	0.1	0.992	7.104	41
12-14	136, 73	7, 11	0.5	-0.1	0.985	9.827	61
14-16	134, 74	13, 8	0.5	-0.1	0.980	11.580	82
16-18	273, 83	18, 2	0.5	0.3	0.989	8.399	41
18-20	149, 82	6, 7	0.5	0	0.991	7.728	71
			Hanging Wall				
0-6, near the Santa Susana fault	105, 0	15, 10	0.5	0.1	0.983	10.533	102
0-6, southwest of the Santa Susana fault	109, 51	31, -9	0.5	0.1	0.986	9.542	68
6-12, above primary rupture	270, -4	0, -6	0.5	-0.1	0.981	11.101	117
0-4, updip of main rupture plane	106, -40	20, 5	0.5	0.1	0.993	6.583	38
4-6, updip of main rupture plane	112, 75	20, 0	0.5	0	0.992	7.163	21

See text for complete descriptions of kinematic variables and misfit values
*Orientations of d_1 and d_3 given as trend, followed by plunge. Positive values of plunge are below the horizontal; negative values are above the horizontal.

is no horizontal extension or contraction parallel to d_2 (i.e., subparallel to the strike of the fault). The few exceptions are from the Sylmar segment (depth intervals 18-20 km and 14-16 km; Table 1) and the Placerita segment (depth interval 6-12 km; Table 2). Inversion of data from these domains shows that $D = 0.6$, which implies that d_2 is somewhat closer in value to d_1 (maximum lengthening) than to d_3 (maximum shortening), and thus the deformation within the primary rupture zone probably accommodates a small component of subhorizontal NW-SE extension parallel to the strike of the fault.

Models for the distribution of coseismic slip directions on the Northridge fault have been made by *Wald et al.* [1996] using a combined analysis of geodetic, teleseismic, and strong motion data and by *Hudnut et al.* [1966] and *Shen et al.* [1966] using inversion of coseismic GPS data. To compare these models with our results, we use the characteristics of the micropolar deformation (i.e., $\boldsymbol{d}_i$, D, and W) that we found by inverting aftershocks from domains along the mainshock rupture plane, and we calculate the direction of the maximum resolved incremental shear along the best fit rupture plane (strike=122°, dip=40° SW). In essence, this analysis finds the orientations on the blind Northridge thrust of the maximum resolved incremental shear for the aftershock deformation. The precision of this orientation is shown on Figure 6 and discussed in the appendix.

Our calculated motions of the hanging wall block (Figure 6) indicate up-to-the-northeast shearing on the blind Northridge thrust, with local components of obliquity. The most distinctive departure from pure dip-slip motion in our model (Figure 6) is the opposite sense of obliquity on opposite sides of the Chatsworth lateral ramp in the depth range of 10-14 km. Specifically, our model predicts left-reverse slip to the southeast of the Chatsworth structure and right-reverse slip to the northwest. *Hudnut et al.* [1996] derived a similar upward diverging pattern of mainshock slip on the primary rupture plane. *Shen et al.* [1996] also modeled obliquity on the primary rupture plane, but their best fit model suggests predominantly left-reverse displacement on both the Placerita and Sylmar segments during the mainshock. In contrast, the model of *Wald et al.* [1996] implies upward converging senses

Table 3. Inversion Results, Newhall-Potrero Segment

Depth, km	d_1 (Maximum Extension)*	d_3 (Maximum Shortening)*	D	W	Mean Cos	Cos^{-1} (Mean Cos)	Number of Data
10-12, northeast dipping events	340, 67	183, 21	0.5	0.2	0.988	8.915	82
12-14, northeast dipping events	302, 73	177, 10	0.5	0.1	0.989	8.516	129
14-16, northeast dipping events	330, 65	198, 17	0.5	0.1	0.991	7.791	52
7-14, southwest dipping events	341, 80	20, -8	0.5	0.3	0.984	10.355	69
0-5 (all)	294, 21	17, -18	0.5	0	0.983	10.724	46

See text for complete descriptions of kinematic variables and misfit values
*Orientations of d_1 and d_3 given as trend, followed by plunge. Positive values of plunge are below the horizontal; negative values are above the horizontal.

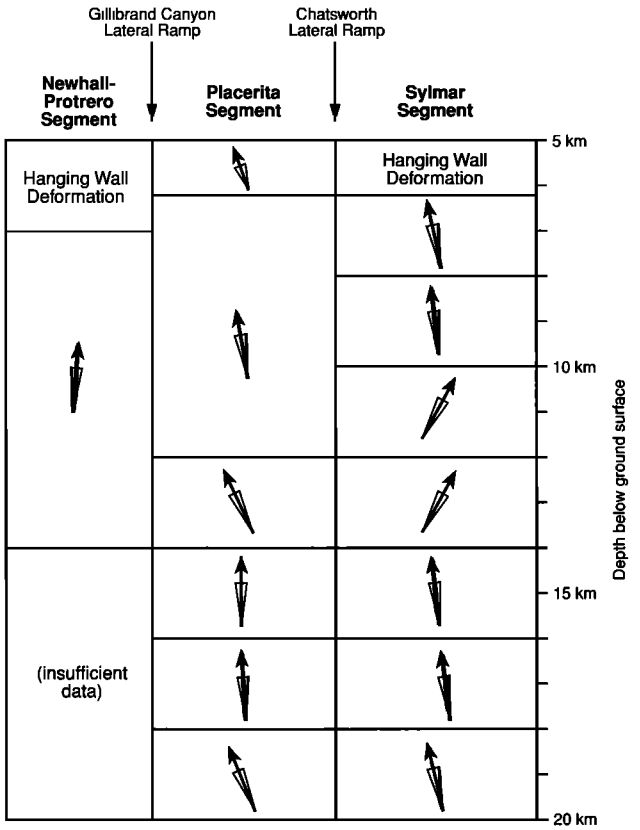

Figure 6. Directions of the maximum resolved incremental shear on the best fit rupture plane of *Wald et al.* [1996], determined from micropolar inversion of aftershock data (Tables 1-3). The vectors shown represent the average direction of slip on the fault associated with the aftershocks for discrete areas of the mainshock rupture plane. The variation of the rake of the maximum incremental shear associated with the precision of the inversion results is approximately ±7.5° and is indicated by the fan-shaped marks on either side of the slip vector. See text for explanation of the derived slip directions. See the appendix for derivation of the precision in the rake of the slip vector.

of obliquity (i.e., generally right reverse slip on the Sylmar segment and left reverse slip on the Placerita segment) during the mainshock. Although different patterns of obliquity are associated with the different models, we find that our results for the aftershock deformation generally are consistent with reverse slip on the primary rupture zone.

To interpret the values of the relative vorticity parameter W obtained from the inversion (Tables 1-3), we first adopt a convention for expressing the sense of large-scale vorticity associated with the southwest-side-up simple shearing along the southwest dipping Northridge thrust. Looking northwest along the strike of the fault, the sense of shear for southwest-side-up motion, and the corresponding vorticity viewed in this direction, is clockwise. Using the right-hand rule, a clockwise vorticity is represented by an axial vector that lies in the fault plane, is normal to the direction of slip, and is positive in the northwest direction. The relative vorticity W parallel to d_2 (equation (2)) is proportional to the difference between the small-scale vorticity of fault-bounded blocks within the primary rupture zone and the large-scale vorticity (equation (2); *Twiss et al.*, [1993] refer to these as the microvorticity and the macrovorticity, respectively). Because we assume that the relative vorticity vector is parallel to the d_2 axis, this requires choosing a right-handed coordinate system where the d_2 axis also is positive in a subhorizontal, northwest direction (Tables 1-3). With this convention, positive or negative values of W in Tables 1-3 imply that the clockwise rotation rate of rigid blocks in the primary blind thrust zone is higher or lower, respectively, than the average clockwise rotation rate of material lines in the large-scale top-northeast simple shearing across the zone.

The inversion results indicate a range in values of the relative vorticity parameter W between -0.2 and 0.3 (Tables 1-3). Zero values of W imply no difference between the large-scale and small-scale vorticities. Because the geometries of the blocks and the seismogenic faults that form their boundaries are not visible, however, it is not possible to determine which class of kinematic models is appropriate to account for the nonzero values of W [see *Twiss et al.*, 1993; *Unruh et al.*, 1996]. Moreover, *Unruh et al.* [1996] found that values of W with an absolute value of 0.2 or less may not be significantly different from zero, based on sensitivity analyses of inversions using aftershock data from the 1992 Landers earthquake. If this is true for the Northridge earthquake aftershocks as well, then only a few of the nonzero values of W are significant (i.e., 14-16 km interval, Sylmar segment; 16-18 km interval, Placerita segment; southwest dipping events between 7 and 14 km, Newhall-Potrero segment), and in general, the relative vorticity along most of the primary rupture zone probably is negligible (Tables 1-3).

7.2. Hanging Wall Deformation From Analysis of Aftershocks

We grouped aftershocks in the hanging wall block of the Northridge thrust fault into depth domains within each of the three major structural segments identified by *Yeats et al.* [1994]. We also identified what appear to be discrete clusters of aftershocks in the hanging wall from cross sections of seismicity (Figures 2 and 3), and we inverted data from these clusters where a sufficient number of focal mechanisms were available to obtain a robust solution.

The inversion results (Tables 1-3; see Figures 2 and 3 for locations of individual domains) generally show that the axis of maximum lengthening (d_1) in the hanging wall for all three structural segments is subhorizontal horizontal NW-SE, in contrast to the approximately vertical orientation of d_1 along the primary rupture zone at depth. For both the hanging wall block and the primary rupture zone, the axis of maximum shortening d_3 is horizontal and oriented northeast-southwest, so the change in deformation style from the primary rupture zone to the hanging wall block is characterized by an exchange in orientation of the d_2 and d_1 axes. Along the Sylmar segment, the transition between vertical d_1 and subvertical d_2 deformation occurs at about 3 km depth (Table 1). For the Placerita segment, the domain of subvertical d_2 includes the upper 4 km of the crust updip of the primary rupture zone and appears to extend to the base of the hanging wall (Table 2). To the northwest, aftershocks from the Newhall-Potrero segment indicate that the transition between subvertical d_1 and d_2 occurs at about 3-5 km depth (Table 3). This difference in the orientations of the principal incremental strain axes can be seen in equal-area stereograms of d_1 and d_3 plotted for the primary rupture zone (Figure 7), and for events that occurred in the hanging wall block or in the upper 4 km of the crust updip of the primary rupture zone (Figure 8).

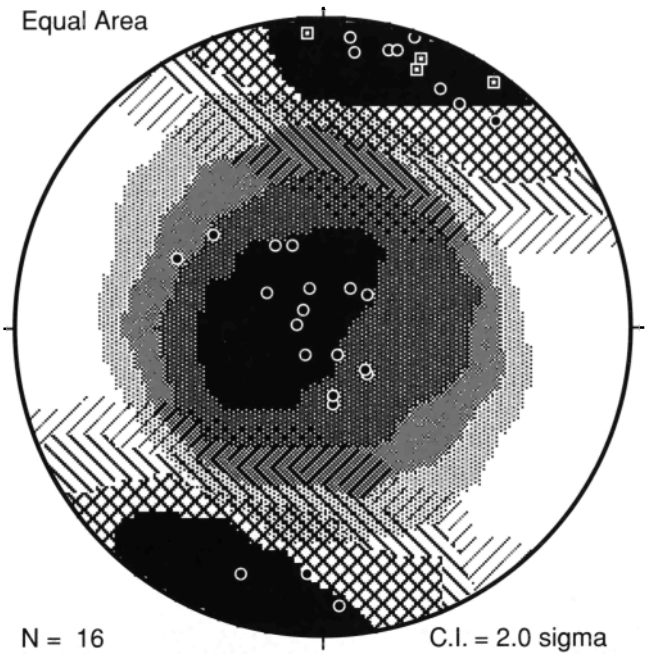

Figure 7. Stereogram showing the orientations of the principal incremental strain axes obtained from inversions of aftershocks along the primary rupture zone. Solid dots show the locations (trend and plunge) of individual principal incremental strains in the lower hemisphere; squares show principal axes that plot in the upper hemisphere (results from 16 inversions plotted; all data taken from Tables 1-3). The Kamb contours of the distribution of the data differentiate the maximum lengthening principal strains (d_1, associated with the stippled contours) from the maximum shortening principal strains (d_3, associated with the striped contours) (contour interval is 2 sigma). Note that for the primary rupture zone, the Kamb contours show that d_1 generally is steeply plunging to subvertical and that d_3 generally is subhorizontal and oriented northeast-southwest.

In general, the value of the deformation rate parameter D for domains in the hanging wall is 0.5 (Tables 1-3), which for a constant volume deformation, characterizes a plane incremental strain such that d_1 (maximum extension) and d_3 (maximum shortening) are equal and opposite in value and that there is no length change in the vertical direction (i.e., parallel to d_2). An exception to this general result is the hanging wall deformation in the upper 6 km of the Placerita segment, southwest of the Santa Susana fault (Table 2). The inversion results indicate that d_3 (maximum shortening) is subhorizontal and directed NE, but that d_1 (maximum lengthening) is plunging approximately 51° to the SE (Table 2). The moderate plunge of d_1 for this domain can be interpreted as reflecting components of lengthening both in the NW-SE direction and in the vertical direction. Assuming constant volume, the aftershocks in this domain accommodate a component of vertical thickening of the hanging wall, in addition to northwest-southeast lengthening and northeast-southwest shortening.

8. Kinematic Model and Interpretation

Our inversions indicate that aftershock deformation associated with the mainshock rupture is consistent with slow, progressive reverse slip, with most of the aftershocks occurring within a tabular zone centered on the Northridge thrust fault. The principal contractional strain (d_3) within this zone is subhorizontal and normal to the strike of the fault; the principal extensional strain (d_1) is subvertical; and the intermediate principal strain (d_2) is subhorizontal and parallel to strike of the fault. In contrast, aftershock deformation in the upper 3-7 km of the hanging wall block is distributed throughout a large volume of the crust and is characterized by subhorizontal shortening (d_3) directed normal to the strike of the Northridge thrust and subhorizontal extension (d_1) parallel to the strike of the Northridge thrust. The intermediate principal strain (d_2) in the hanging wall block is subvertical, as opposed to subhorizontal along the mainshock rupture plane. Based on values of the deformation parameter D obtained from the aftershock inversions, the shortening and lengthening incremental strains in the hanging wall block are approximately equal and opposite in magnitude, and there is negligible vertical thinning or thickening. The different deformation styles of the mainshock rupture zone and the hanging wall are illustrated schematically in a block diagram (Figure 9).

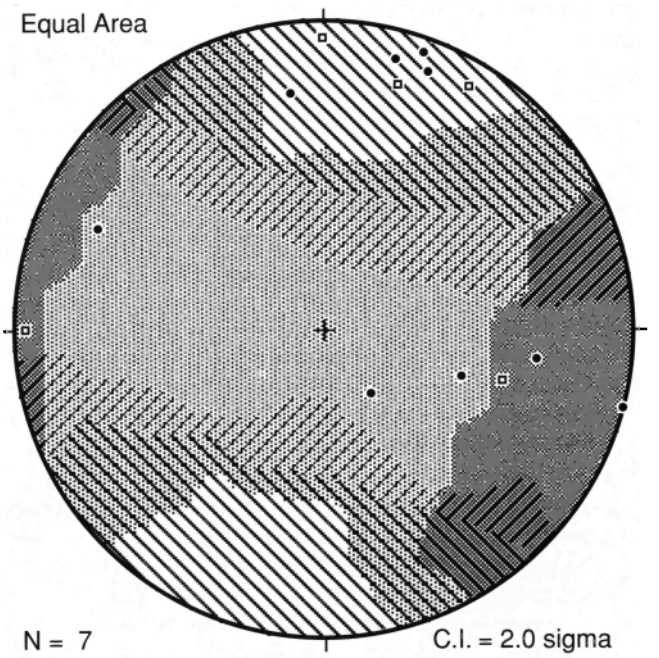

Figure 8. Stereogram showing the orientations of the principal incremental strain axes obtained from inversions of aftershocks in the upper 6 km of the hanging wall block. Solid dots show the locations (trend and plunge) of individual principal incremental strains in the lower hemisphere; squares show principal axes that plot in the upper hemisphere (results from seven inversions plotted; all data taken from Tables 1-3). Kamb contours of the distribution of the data differentiate the maximum lengthening principal strains (d_1, associated with the stippled contours) from the maximum shortening principal strains (d_3, associated with the striped contours) (contour interval is 2 sigma). The orientations of d_3 form a distinct, subhorizontal maximum oriented northeast-southwest, similar to the inversions of aftershocks from the primary rupture zone. Unlike the primary rupture zone data (Figure 7), however, the directions of maximum lengthening (d_1) from inversions of hanging wall aftershocks form subhorizontal to moderately plunging maxima, indicating significant components of fault-parallel extension.

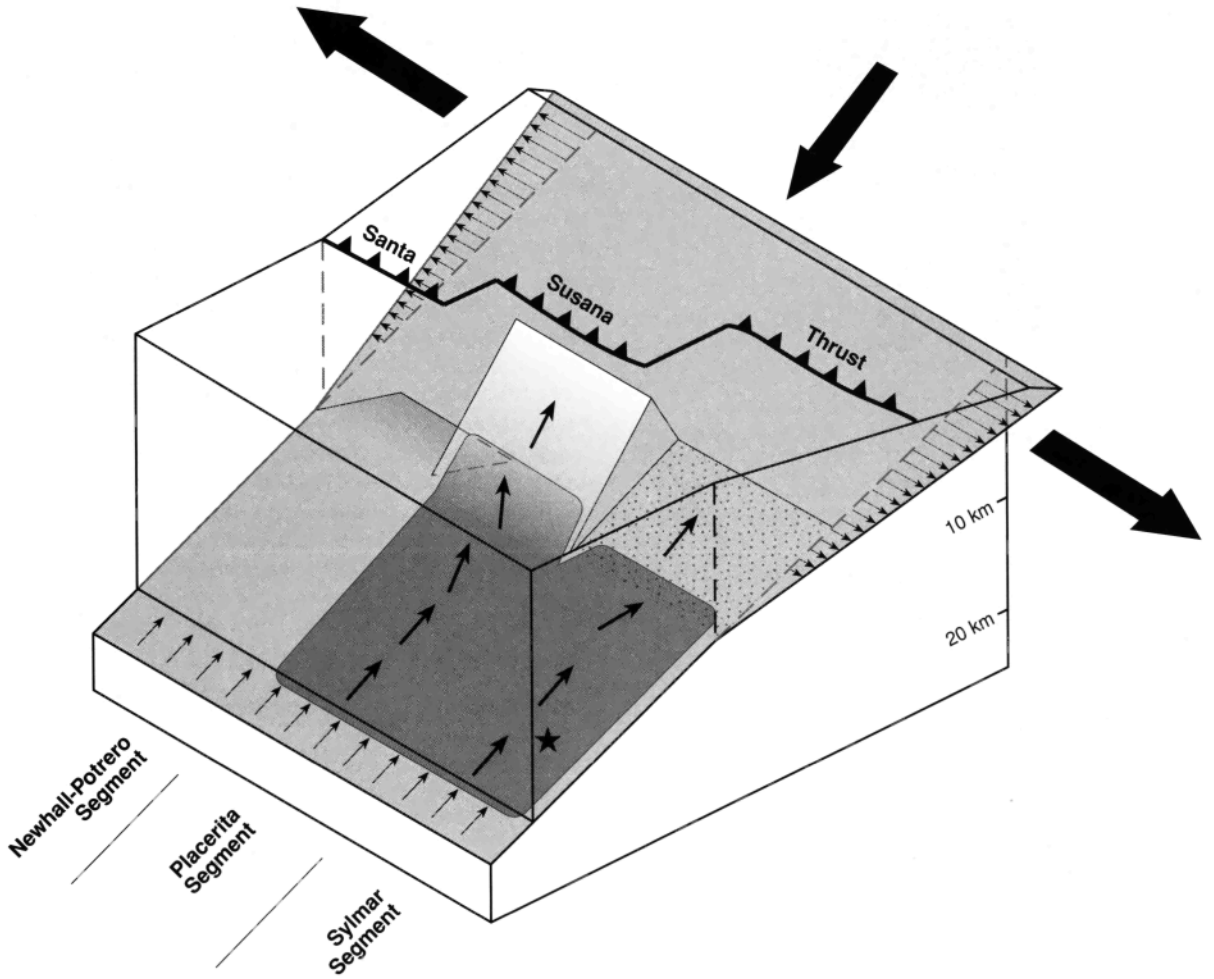

Figure 9. Schematic block diagram illustrating geometry of the primary rupture zone and the kinematics of uplift and deformation of the hanging wall accommodated by the Northridge earthquake aftershocks. Star shows approximate location of mainshock. Darker shaded area within the Placerita and Sylmar segments shows area of rupture plane where most of the coseismic strain release occurred (from data of *Wald et al.* [1996]). The variations in geometry of the primary rupture zone in the diagram are inferred primarily from cross-sections of seismicity and structure contours of the base of the aftershock zone [*Hauksson et al.*, 1995]. Arrows on the primary rupture zone schematically show the variations in the average slip direction as indicated by the forward modeling of the inversion results (Figure 6 presents a detailed model of aftershock slip directions). In particular, note that the aftershock slip directions for the Placerita and Sylmar segments diverge across the Chatsworth lateral ramp boundary. The approximately pure shear, plane strain deformation of the hanging wall block is indicated by the arrows showing the horizontal shortening and lengthening directions and schematically by the upward flaring of the hanging wall block parallel to the strike of the Northridge thrust, which indicates a relative increase in fault-parallel lengthening with decreasing depth.

These results generally are consistent with geodetic observations of postseismic deformation in the epicentral region of the Northridge earthquake. Based on analysis of GPS data, *Donnellan and Lyzenga* [1996] reported that reverse slip on the Northridge thrust fault continued for several months following the mainshock. They further noted geodetic evidence for postmainshock deformation of the upper 5 km of the crust, which approximately coincides with the depth range of most of the aftershocks in the hanging wall block. According to *Donnellan and Lyzenga* [1996], the moment release equivalent of the combined afterslip on the Northridge thrust and postmainshock deformation of the upper crust is approximately M6.2, which represents approximately 20% of the total moment release associated with the M_w 6.7 mainshock.

The mainshock rupture and the associated deformation, including the fault-parallel lengthening measured by GPS geodesy, can be successfully modeled [e.g., *Hudnut et al.*, 1996] as an elastic dislocation on the blind Northridge thrust fault, which is reflected in the upper crust as an elastic horizontal shortening normal to the fault strike and an elastic lengthening parallel to strike (Figure 5). The distributed aftershock deformation, however, can, at a sufficiently large scale, be viewed as a quasi-continuous "seismic flow" [see *Kostrov*, 1974], or a quasi-ductile deformation. Our inversions of the aftershock focal mechanisms together with the postmainshock geodetic analysis of *Donnellan and Lyzenga* [1996] show that thrusting motion continued along the mainshock rupture zone and that the deformation in the hanging wall block was characterized by an inhomogeneous

pure shear (a plane strain) with shortening normal to the fault strike and lengthening parallel to strike. Thus the deformation accommodated by the mainshock continued during the aftershock sequence as a quasi-ductile flow with essentially unchanged geometry.

This flow can be explained either as a quasi-ductile continuation of the coseismic deformation or as a relaxation phenomenon, as further discussed below. The slow reverse afterslip on the Northridge thrust following the mainshock is not consistent with highly reoriented stresses near a fault on which the stress drop is assumed to be nearly complete, nor is it consistent with elastic rebound following dynamic overshoot of fault displacement during the mainshock rupture. We propose two hypotheses to explain the afterslip along the main rupture zone (see *Scholz* [1990, section 5.2.2] for a brief review):

1. The upper crust, including the depth range of about 10-20 km where most of the coseismic strain was released during the Northridge mainshock, behaves as a brittle-elastic material that can undergo quasi-ductile flow. Both the strain accumulation prior to the earthquake, as well as the coseismic deformation of the hanging wall block above the blind fault, can be modeled by adopting an elastic constitutive relation for the upper crust. The afterslip and aftershock activity along the mainshock rupture zone could represent a quasi-ductile release of part of the remaining elastic strain that was not released during the mainshock. This model implies a strain weakening of the material in the fault zone because the continued quasi-ductile deformation occurs in a stress field whose magnitude must have decreased due to release of strain during the main shock.

2. The upper crust could have layered mechanical properties characterized by a brittle-elastic layer overlying a ductile-elastic layer. The boundary between these two layers could coincide with the local brittle-ductile transition in this part of the western Transverse Ranges, with earthquakes and aftershocks primarily confined to the upper layer. In this model, assuming constant velocity boundary conditions, the progressively increasing displacement on the boundary would have built up elastic stresses in both crustal layers prior to an earthquake. Presumably the stress would be higher in the brittle-elastic layer than in the ductile-elastic layer, because ductile flow in the latter would progressively relax part of the stress. The loss of cohesion in the upper brittle-elastic layer associated with a large earthquake would have temporarily and locally decreased the stress in the upper layer and thereby increased the stress in the lower layer. This increase of stress in the lower layer would drive an increase in the rate of ductile flow; this in turn would relax the stresses concentrated there and drive continued reverse slip in the overlying weakened mainshock rupture zone, producing aftershock activity. Presumably, the mainshock rupture zone and the upper crustal layer eventually recover all or part of the original elastic strength, possibly through a process of static hardening, and the process of elastic strain accumulation averaged over both layers begins again.

Above the blind fault tip, the standard Coulomb failure criterion suggests that the shallow crust must be relatively weak and thus would support a relatively small stress before the mainshock event. After the mainshock event, the deformation in the shallow crust above the tip of the blind thrust stress would increase and initiate the process of quasi-ductile flow.

Such a qualitative analysis cannot restrict the rheology of the crust precisely. Nevertheless, a few conclusions are possible. A simple elastic crustal rheology of the type used to model the surface deformation associated with the mainshock is not sufficient to explain the occurrence, distribution, and style of the observed aftershock deformation, either along the mainshock rupture plane or in the hanging wall block of the Northridge thrust fault. The upper crust must be a brittle-elastic material that can deform by quasi-ductile flow; it must be a strain-weakening material because the deformation initiated by the main shock continues after the associated stress drop; and it must have a fading memory because its strength must recover with time following the deformation. Finally, a simple relaxation process of converting transient elastic strain into permanent ductile deformation at constant total strain is inconsistent with the geodetic evidence of continuing deformation. There must be greater complexity than is implied by such a relaxation model in either the constant total-strain boundary conditions or in the rheology of the material.

9. Implications for Kinematic Models of Basement-Involved Folding

The coseismic and postseismic deformation of the hanging wall observed during the Northridge earthquake depart significantly from the assumptions of kinematic models for basement-involved folding by *Narr and Suppe* [1994]. These models assume conservation of area in a plane containing the slip direction and the normal to the thrust fault, and they predict that the horizontal component of motion of material points in the hanging wall is parallel to the horizontal component of slip on the fault at depth. This assumption is inconsistent with the fault-parallel extension of the hanging wall during the Northridge earthquake. The kinematic models further assume that deformation of the hanging wall is limited to rigid body translation, except where material points pass through axial surfaces, which are kink band boundaries that are fixed to changes in dip of the fault at depth. As material passes through these surfaces, it is deformed by localized shearing. Our results clearly show, however, that the pure shear deformation is distributed throughout the hanging wall and is not limited to axial surfaces of the northeast vergent fault propagation fold identified by *Davis and Namson* [1994] and *Huftile and Yeats* [1996] above the blind Northridge thrust.

As earthquakes occur on different segments of the Northridge thrust fault, it is possible that the fault-parallel extensions may average out to zero, and thus the assumptions of the *Narr and Suppe* [1994] model may be appropriate for evaluating finite deformation. In fact, *Narr and Suppe* [1994] successfully modeled the development of several basement-involved anticlines in the southern Rocky Mountains using the assumptions described above. If the hanging wall and primary rupture zone of the Northridge thrust fault were exposed by erosion similar to the basement-involved structures in the southern Rocky Mountains, however, brittle shear sense indicators on small faults in the hanging wall would retain a record of the average horizontal pure shear strain accommodated by the postmainshock deformation. Presumably, therefore, some record of the permanent fault-parallel lengthening would be retained in the relatively small brittle faults in the hanging wall. This out-of-plane motion or transfer of material must be accounted for to develop rigorous,

area-balanced cross sections, especially if large earthquakes occur repeatedly on, or are limited to, discrete rupture segments in the blind thrust system.

The example of the Northridge earthquake indicates that more general kinematic models for fault-related folding are needed to account for the coseismic elastic deformation of the hanging wall, and the accumulation of some permanent distributed brittle deformation by aftershock activity. For example, the trishear model of *Erslev* [1991] posits that localized shearing along the main thrust at depth may be distributed updip in a triangular shear zone. Depending on the geometry of the shear zone, conservation of volume may require out-of-plane or fault-parallel transfer of material. In particular, if the triangular shear zone is primarily contained in the hanging wall block, mass conservation requires out-of-plane transfer of material away from the shear zone [see *Erslev*, 1991, Figure 2a). Thus the trishear model potentially provides a kinematic explanation for the fault-parallel extension observed during the Northridge earthquake that is consistent with the ductile-elastic model discussed above.

10. Conclusions

Based on inversion of aftershock data, deformation that occurred at depths below about 6 km and is associated with the primary rupture zone is consistent with slow, progressive, postmainshock reverse slip in a southwest dipping thrust fault zone. In contrast, inversion of aftershocks from the upper 5-7 km of the hanging wall block directly above the blind thrust fault shows that the seismogenic deformation can be described as an approximately horizontal inhomogeneous pure shear deformation, characterized by horizontal NE-SW shortening and horizontal NW-SE extension.

Deformation in both regions includes a component of permanent quasi-ductile flow of a brittle-elastic material. Along the fault zone at least, this material must be a strain-weakening material with fading memory. A two-layer model of a brittle-elastic layer overlying a ductile-elastic layer could account for the observed deformation, but a simple relaxation process by which transient elastic deformation is converted by quasi-ductile flow to permanent deformation at constant total strain cannot account for the observed progressive accumulation of strain after the main shock event.

We propose that slip on the blind thrust during the mainshock transferred an inhomogeneous, horizontal pure shear strain to the hanging wall block and that part of this deformation was accommodated by slow, quasi-ductile "seismic flow" which is characterized by distributed brittle faulting. The patterns of mainshock and aftershock deformation indicate that kinematic models for incremental fault-related folding in crystalline basement terranes must be general enough to account for the observed three-dimensional deformation (i.e., fault-parallel extension) of the hanging wall block in order to be useful for predicting patterns of coseismic surface deformation.

Appendix: Sensitivity of the Derived Slip Directions to the Precision of the Inversion Results

As discussed in the text, we use the parameters of the best fit model obtained from the aftershock inversions to evaluate the direction of the maximum incremental shear on the blind Northridge thrust (Figure 6). We interpret this vector to show the average direction of postseismic slip on the fault associated with the aftershock activity. At present, we cannot evaluate the statistical uncertainty in the rake of this slip vector; however, we can evaluate the sensitivity of this vector to the precision of our inversions. In the following example, we test the sensitivity of modeled aftershock slip direction on the Northridge thrust (Figure 6) by systematically varying the model parameters used in the inversions.

As discussed in the text, the orientations of the best fit principal strain rate axes are bracketed within grid increments of 5°, and the best fit values of the parameters D and W are bracketed to within 0.1 grid increments. This is equivalent to a precision of ± 2.5° for the principal strain rate axes and a precision of ± 0.05 for the values of D and W. For the following analysis, we used the inversion results for the 12-14 km depth range of the Sylmar segment of the Northridge thrust as a test case. Using our grid-search algorithm PTGRDSRCH, we generated a typical suite of grid models by varying the orientation of the best fit principal axes by 2.5° grid increments. Given the precision of our inversion results, a model with a lower misfit value could be found among this suite of models. We then evaluated the direction of resolved incremental shear on the best fit fault plane of *Wald et al.* [1996]; (strike of 122°, dip of 40°SW) for each of these models, holding the values of D and W constant. The results indicate that for a variation of ±2.5° in the orientation of the principal strain rate axes, the rake of the maximum incremental shear vector on the Northridge thrust varies by ±5° from the rake of the vector for our best fit model. Similarly, we evaluated the variation in the rake as a function of varying D by 0.05 grid increments, holding the orientation of the principal strain rate axes and the value of W constant. For a variation of ±0.05 in the value of D, the rake varies by ±2°. For W, we use ±0.1 for the sensitivity test instead of ±0.05 to evaluate the maximum variation in the rake because previous sensitivity tests by *Unruh et al.* [1996] show that the misfit is less sensitive to variations in W than in $\boldsymbol{d}_t$ or D. For a variation of ±0.1 in the value of W, the rake varies by ±0.5°. By conservatively combining the variation in the rake associated with the precision of all the individual model parameters, the minimum precision of the rake on the fault plane is ±7.5°.

Acknowledgments. We are indebted to Richard Allmendinger for the use of his program Stereonet 4.9.5, which we used to plot and contour our orientational data. Comments on an earlier draft of this paper by E. Erslev, G. Huftile, and an anonymous reviewer led to significant improvements in the presentation of the data and analyses. The present paper was improved by critical reviews from K. Hudnut, W. Prescott, and J. Gomberg. Support for this research was provided by the National Science Foundation through grants EAR-9416318 and EAR-9526105 to J.R.U. and EAR-9219633 to R.J.T.

References

Davis, T. L., and J. S. Namson, A balanced cross-section of the 1994 Northridge earthquake, southern California, *Nature*, *372*, 167-169, 1994.

Donnellan, A., and G. A. Lyzenga, Northridge postseismic deformation: inferences from continuous and campaign GPS observations, *Eos Trans. AGU*, *77*(46), Fall Meet. Suppl., F147, 1996.

Eringen, A. C., Linear theory of micropolar elasticity, *J. Math. Mech.*, *15*, 909-924, 1966.

Eringen, A. C., Theory of micropolar fluids, *J. Math. Mech.*, *16*, 1-18, 1967.

Erslev, E. A., Trishear fault-propagation folding, *Geology*, *19*, 617-620, 1991.

Hauksson, E., and J. S. Haase, Three-dimensional V_p and V_p/V_s models of the Los Angeles basin and central Transverse Ranges, California, *J. Geophys. Res.*, *102*, 5423-5453, 1997.

Hauksson, E., L. M. Jones, and K. Hutton, The 1994 Northridge earthquake sequence in California: Seismological and tectonic aspects, *J. Geophys. Res.*, *100*, 12,335-12,355, 1995.

Hudnut, K. W., Z. Shen, M. Murray, S. McClusky, R. King, T. Herring, B. Hager, Y. Feng, P. Fang, A. Donnellan and Y. Bock, Co-seismic displacements of the 1994 Northridge, California, earthquake, *Bull. Seismol. Soc. Am.*, *86*(1b), S19-S36, 1996.

Huftile, G., and B. Yeats, Deformation rates across the Placerita (Northridge *Mw*=6.7 aftershock zone) and Hopper Canyon segments of the western Transverse Ranges deformation belt, *Bull. Seismol. Soc. Am.*, *68*(1b), S3-S18, 1996.

Jennings, C. W., and R. G. Strand, Geologic map of California, Los Angeles sheet, scale 1:250,000, *Calif. Div. of Mines and Geol.*, Sacramento, 1969.

Kostrov, V. V., Seismic moment and energy of earthquakes, and seismic flow of rock, *Izv. Acad. Sci. USSR Phys. Solid Earth*, Engl. Transl., no. 1, 23-44, 1974.

Narr, W., and J. Suppe, Kinematics of basement-involved compressive structures, *Am. J. Sci.*, *294*(7), 802-860, 1994.

Scholz, C. H., *The Mechanics of Earthquakes and Faulting*, Cambridge Univ. Press, New York, 1990.

Shen, Z.-K., B. X. Ge, D. D. Jackson, D. Potter, M. Cline, and L.-Y. Sung, Northridge earthquake rupture models based on the Global Positioning System measurements, *Bull. Seismol. Soc. Am.*, *86*(1b), S37-S48, 1996.

Twiss, R. J., and E. M. Moores, *Structural Geology*, 532 pp., W.H. Freeman, New York, 1992.

Twiss, R. J., G. M. Protzman, and S. D. Hurst, Theory of slickenline patterns based on the velocity gradient tensor and microrotation, *Tectonophysics*, *186*, 215-239, 1991.

Twiss, R. J., B. J. Souter, and J. R. Unruh, The effect of block rotations on the global seismic moment tensor and patterns of seismic *P* and *T* axes, *J. Geophys. Res.*, *98*, 645-674, 1993.

Unruh, J. R., R. J. Twiss, and E. Hauksson, Seismogenic deformation field in the Mojave block and implications for the tectonics of the eastern California shear zone, J. Geophys. Res., 101, 8335-8362, 1996.

Wald, D. J., T. H. Heaton, and K. W. Hudnut, The slip history of the 1994 Northridge, California, earthquake determined from strong motion, teleseismic, GPS and leveling data, *Bull. Seismol. Soc. Amer.*, *86*(1b), S49-S70, 1996.

Yeats, R. S., Late Cenozoic structure of the Santa Susana fault zone, *U.S. Geol. Surv. Prof. Pap.*, *1339*, 137-160, 1987.

Yeats, R. S., and G. J. Huftile, The Oak Ridge fault system and the 1994 Northridge earthquake, *Science*, *373*, 418-420, 1995.

Yeats, R. S., G. J. Huftile, and L. T. Stitt, Late Cenozoic tectonics of the east Ventura basin, Transverse Ranges, California, *AAPG Bull.*, *78*(7), 1040-1074, 1994.

E. Hauksson, Seismological Laboratory, California Institute of Technology, Mail Code 252-21, 1200 E. California Blvd., Pasadena, CA 91125. (e-mail: hauksson@gps.caltech.edu)

R. J. Twiss, Department of Geology, University of California, Davis, CA 95616-8605. (e-mail: twiss@geology.ucdavis.edu)

J. R. Unruh, William Lettis & Associates, 1777 Botelho Dr., Suite 262, Walnut Creek, CA 94596. (e-mail: unruh@lettis.com)

(Received February 11, 1997; revised July 15, 1997; accepted July 29, 1997.)